

Analysis of the non-periodic oscillations of a self-excited friction-damped system with closely-spaced modes

Lukas Woiwode (✉ lukas.woiwode@ila.uni-stuttgart.de)

University of Stuttgart: Universitat Stuttgart

Alexander F. Vakakis

University of Illinois at Urbana-Champaign

Malte Krack

University of Stuttgart: Universitat Stuttgart

Research Article

Keywords: utter, nonlinear vibration, non-periodic solution, nonlinear modes, modal interaction, averaging

Posted Date: April 5th, 2021

DOI: <https://doi.org/10.21203/rs.3.rs-269887/v1>

License:  This work is licensed under a Creative Commons Attribution 4.0 International License.

[Read Full License](#)

Version of Record: A version of this preprint was published at Nonlinear Dynamics on October 1st, 2021.

See the published version at <https://doi.org/10.1007/s11071-021-06893-3>.

Analysis of the non-periodic oscillations of a self-excited friction-damped system with closely-spaced modes

Lukas Woiwode (✉)^a

Alexander F. Vakakis^b

Malte Krack^c

^a University of Stuttgart, Stuttgart, Germany, e-mail: Lukas.Woiwode@ila.uni-stuttgart.de

^b University of Illinois at Urbana – Champaign, Urbana, USA

^c University of Stuttgart, Stuttgart, Germany

Abstract

It is widely known that dry friction damping can bound the self-excited vibrations induced by negative damping. The vibrations typically take the form of (periodic) limit cycle oscillations. However, when the intensity of the self-excitation reaches a condition of maximum friction damping, the limit cycle loses stability via a fold bifurcation. The behavior may become even more complicated in the presence of any internal resonance conditions. In this work, we consider a two-degree-of-freedom system with an elastic dry friction element (Jenkins element) having closely spaced natural frequencies. The symmetric in-phase motion is subjected to self-excitation by negative (viscous) damping, while the symmetric out-of-phase motion is positively damped. In a previous work, we showed that the limit cycle loses stability via a secondary Hopf bifurcation, giving rise to quasi-periodic oscillations. A further increase of the self-excitation intensity may lead to chaos and finally divergence, long before reaching the fold bifurcation point of the limit cycle. In this work, we use the method of Complexification-Averaging to obtain the slow flow in the neighborhood of the limit cycle. This way, we show that chaos is reached via a cascade of period doubling bifurcations on invariant tori. Using perturbation calculus, we establish analytical conditions for the emergence of the secondary Hopf bifurcation and approximate analytically its location. In particular, we show that non-periodic oscillations are the typical case for prominent nonlinearity, mild coupling (controlling the proximity of the modes) and sufficiently light damping. The range of validity of the analytical results presented herein is thoroughly assessed numerically. To the authors' knowledge, this is the first work that shows how the challenging Jenkins element can be treated formally within a consistent perturbation approach in order to derive closed-form analytical results for limit cycles and their bifurcations.

Keywords: flutter, nonlinear vibration, non-periodic solution, nonlinear modes, modal interaction, averaging

Symbols and abbreviations

Latin letters

a	amplitude
$a_{1,\max/\min}$	max/min amplitude
d	differential
d_{eq}	equivalent damping of Jenkins element
f	generic function
$f_{0,1,2}$	power series coefficients
f_t	generated force of Jenkins element
i	imaginary unit $\sqrt{-1}$
k_{eq}	equivalent stiffness of Jenkins element
t	time
x	generalized coordinate
\boldsymbol{x}	vector of unknowns of first order system
\mathcal{D}	Poincare section w.r.t. slow time scale
E_{mech}	mechanical energy
\mathcal{O}	order (perturbation)
\mathcal{S}	Poincare section w.r.t. fast time scale
<i>Sub-, superscripts, operators</i>	
$\dot{\square}$	derivative with respect to time
$\hat{\square}$	fixed point solution
$\overline{\square}$	mean-free value
$\overline{\square}$	normalized parameter
$\ \square\ $	euclidian norm
$ \square $	determinant
$[\square]$	dependency on time history

Greek letters

$\Delta\theta$	phase lag of oscillators
ε	small parameter
γ	friction intensity
κ	coupling stiffness
λ	eigenvalue of Jacobian
ω	oscillation frequency
ω^{st}	natural frequency for sticking slider
ω^{sl}	natural frequency for frictionless sliding
$\tilde{\omega}$	energy-dependent natural frequency
ρ	amplitude ratio
τ^*	stick-slip transition time
θ	phase of oscillator
ν	parameter ratio
$\xi_{1,2}$	in-phase/out-of-phase damping
$\xi_{1,\text{div}}$	bifurcation yielding divergence
$\xi_{1,\text{fold}}$	fold bifurcation point
$\xi_{1,\text{Hopf}}$	secondary Hopf bifurcation
$\xi_{1,\text{Hopf}}^{\text{start/end}}$	predicted secondary Hopf bifurcations

Abbreviations

CX-A	Complexification-Averaging (method)
LCO	limit cycle oscillation
LTO	limit torus oscillation
2DOF	two degree-of-freedom-system

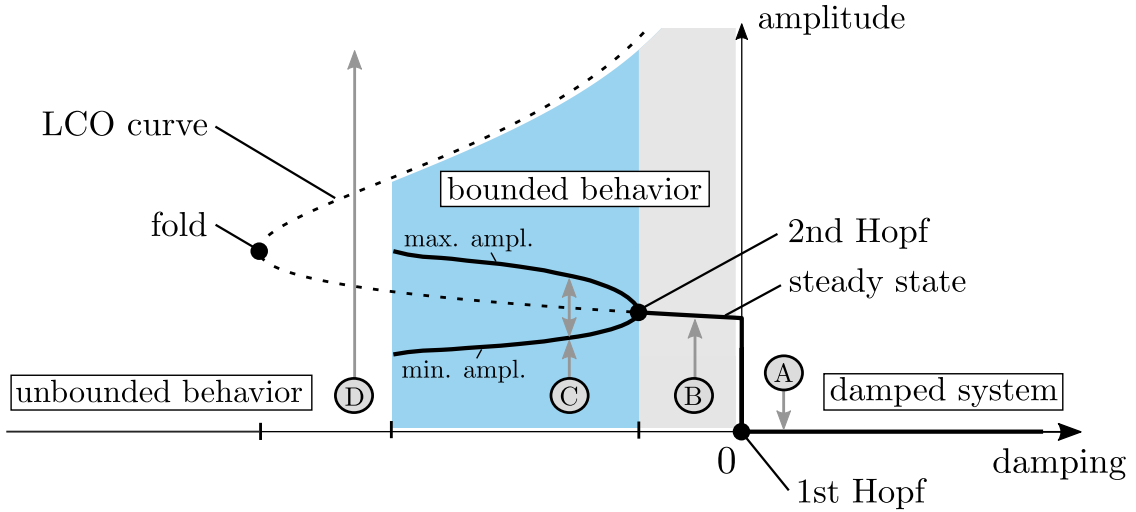


Figure 1: Self-excited friction-damped system with closely-spaced modes: Bifurcation diagram of vibration amplitude vs. viscous damping. LCO curve ('black', 'dashed'), steady state solutions ('black', 'solid') and areas of bounded behavior ('blue' and 'grey'). Arrows indicate increasing and decreasing vibration levels.

1. Introduction

Mechanical systems usually consist of several substructures assembled by joints in which nonlinear contact interactions inevitably occur [1]. The dissipative dry frictional interactions often provide the dominant contribution to the overall energy dissipation in the mechanical system [2]. Friction damping is the motivation to add mechanical joints in some applications, as in the case of under-platform dampers used to mitigate vibrations of turbine blades [2]. Sinha and Griffin [3] were the first to show that friction damping can be used to bound otherwise unstable self-excited vibrations caused by negative (viscous) damping. In case of negative damping of a single mode and well-separated eigenfrequencies, the amplitude-dependent friction damping leads to periodic limit cycle oscillations (LCO). If the negative damping exceeds the point of maximum friction damping, a fold bifurcation occurs such that the LCO becomes unstable giving rise to divergent behavior. The dynamics may become even more complicated when several modes are subjected to negative damping. Based on a simplified model of an aerodynamically unstable rotor stage, the stability limit of LCOs was determined by generalized energy relations based on an averaging technique [4]. However, the bifurcation type associated with the stability limit was not addressed in these works.

It is well-known that friction nonlinearity can trigger modal interactions in the presence of internal resonance conditions (e.g. 1:1 or 1:3 resonances). In [5], we studied numerically a friction-damped two-degree-of-freedom (2DOF) system subjected to negative viscous damping. In Fig. 1, the characteristic behavior for the case of closely-spaced modes (near 1:1 internal resonance) is illustrated in a schematic bifurcation diagram with the viscous damping being considered as control parameter. The trivial case of positive damping leads to exponentially decaying oscillations that approach the static equilibrium position (A). Going from positive to negative damping induces a Hopf bifurcation, causing dynamic instability of the static equilibrium. The vibrations grow until dissipative sliding friction compensates the self-excitation and an LCO is formed from the dynamical balance (B). A secondary Hopf bifurcation causes the loss of periodicity of the LCO beyond a critical level of negative damping, as indicated by the splitting of maximum and minimum steady-state vibration amplitudes (C). Then, the oscillations take the form of limit torus oscillations (LTOs) at first, much in line with the well-known case of coupled van-der-Pol oscillators. More severe negative damping may introduce chaos. Finally, the non-periodic attractor collapses yielding divergent behavior well before the fold bifurcation of the LCO (D) is reached. These findings imply that the common practice to compute only the LCOs (using, e.g., Harmonic Balance and numerical continuation), without properly analyzing their

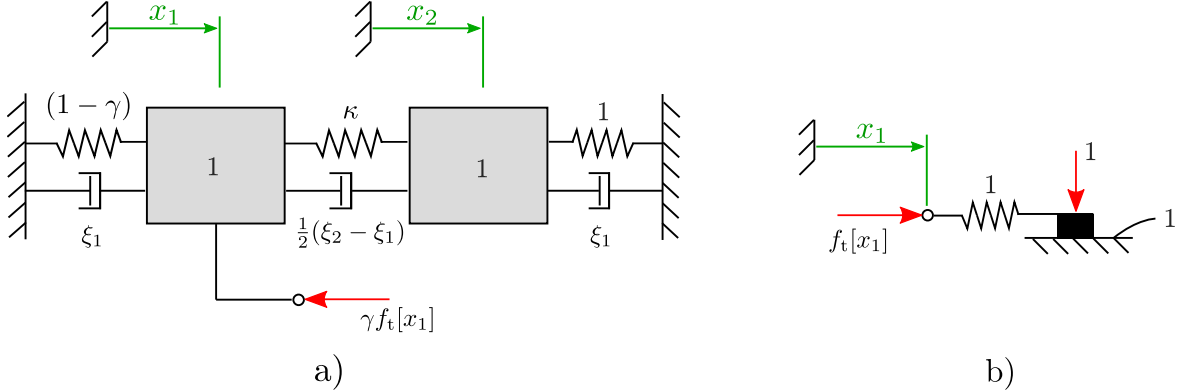


Figure 2: (a) 2DOF model considering in-phase ξ_1 and out-of-phase damping ξ_2 and (b) Jenkins element.

stability, may lead to incomplete modeling of the nonlinear dynamics, and, hence, to potentially dangerous design decisions in practical applications.

In this work, we seek to better understand the emergence of the non-periodic oscillations encountered in [5] for the case of closely-spaced modes. In particular, we would like to establish conditions for the secondary Hopf bifurcation and analyze how the quasi-periodic oscillations further bifurcate into chaos. In the analytical development, the key challenge is the treatment of the Jenkins element¹. To the authors' knowledge, this is the first work that shows how a consistent perturbation approach can be formally applied to analyze this nonlinearity in order to derive closed-form analytical expressions for the emergence of LCOs and their bifurcations.

The article is structured as follows: In Section 2 we describe the investigated 2DOF system. In Section 3, we use averaging to derive an approximation for the slow flow dynamics in the neighborhood of the LCO. In Section 3.3, we analyze the transition from limit torus oscillations to chaotic oscillations. In Section 4, we focus on the secondary Hopf bifurcation and use perturbation calculus to establish the conditions leading to limit torus oscillations. We end this work with some concluding remarks, summarizing the main contributions and providing some related open problems that can be further investigated.

2. Model description

We investigate a 2DOF oscillator (see Fig. 2a), consisting of two unity masses coupled via linear springs in parallel to viscous damper elements. The nonlinear dry friction force acting on the first oscillator is modeled by a Jenkins element, see Fig. 2b. The equations of motion are then given through

$$\ddot{x}_1 + \frac{1}{2}(\xi_1 + \xi_2)\dot{x}_1 + \frac{1}{2}(\xi_1 - \xi_2)\dot{x}_2 + (1 - \gamma)x_1 + \kappa(x_1 - x_2) + \gamma f_t[x_1] = 0, \quad (1)$$

$$\ddot{x}_2 + \frac{1}{2}(\xi_1 + \xi_2)\dot{x}_2 + \frac{1}{2}(\xi_1 - \xi_2)\dot{x}_1 + x_2 + \kappa(x_2 - x_1) = 0, \quad (2)$$

where x_1 and x_2 indicate the generalized coordinates and $\dot{\cdot}$ indicates derivative with respect to time t . The nonlinear friction force $f_t[x_1]$ is defined by the hysteretic differential law

$$df_t = \begin{cases} dx_1 & \|f_t + dx_1\| < 1 \\ 0 & \text{otherwise} \end{cases}, \quad (3)$$

where the dependency on time history is indicated by the operator $[\cdot]$. The friction intensity acting on the first oscillator is controlled by the parameter γ . A similar system was obtained by non-dimensionalization

¹also known as elastic dry friction or elastic Coulomb friction element

in [5].

Note that if the friction element is sticking, the system is linear and fully symmetric. Thus, the linear modes of vibration correspond to symmetric in-phase and out-of-phase motions. For $\kappa \ll 1$ (i.e., for weak coupling between oscillators) the linear natural frequencies are closely-spaced. More specifically, the ratio of the natural frequencies equals $\sqrt{1+2\kappa}$ [5]. The (weak) damper coefficients are designed such that ξ_1 is associated with the symmetric in-phase and ξ_2 with the symmetric out-of-phase motion, indicating proportional damping distribution in the system. Throughout this paper, we set $\xi_1 < 0$ and $\xi_2 > 0$. For sufficiently large vibrations, the force in the friction element saturates, which leads to nonlinear stick-slip behavior and generally asymmetrical behavior.

3. Analysis of the slow dynamics in the neighborhood of the limit cycle

In the following, we gain deeper understanding of the dynamics by analyzing the slow dynamics of the system near the LCO. To this end, we use the Complexification-Averaging (CX-A) method [6]. Of particular interest is the bifurcation point of the first LCO stability loss, i.e., the secondary Hopf bifurcation point, giving rise to LTOs. Furthermore, the transition process from the LTOs to chaos will be analyzed.

3.1. Extraction of the slow dynamics using CX-A

To this end, we introduce the following ansatz,

$$x_j(t) \approx \Re\{a_j(t)e^{i\theta_j(t)}e^{i\int \omega dt}\}, \quad (4)$$

where $\Re\{\cdot\}$ denotes the real part and $i = \sqrt{-1}$. The dynamics in terms of x_1, x_2 is decomposed into a fast oscillation with the instantaneous (fast) oscillation frequency ω (which is treated an independent free parameter) and a slow modulation of amplitude a_j and phase θ_j , see e.g. [6]. Under the assumption of well-separable time scales, averaging over the fast dynamics leads to a set of explicit first order differential equations for the slow dynamics,

$$\dot{a}_1 = -\frac{1}{2\omega} \left(\kappa a_2 \sin(\theta_1 - \theta_2) + \frac{1}{2}(\xi_1 - \xi_2)\omega a_2 \cos(\theta_1 - \theta_2) + \frac{1}{2}(\xi_1 + \xi_2)\omega a_1 + \gamma \omega d_{\text{eq}}(a_1) a_1 \right), \quad (5)$$

$$\dot{\theta}_1 = -\frac{1}{2a_1\omega} \left(\kappa a_2 \cos(\theta_1 - \theta_2) - \frac{1}{2}(\xi_1 - \xi_2)\omega a_2 \sin(\theta_1 - \theta_2) - (-\omega^2 + \kappa - \gamma + \gamma k_{\text{eq}}(a_1) + 1) a_1 \right), \quad (6)$$

$$\dot{a}_2 = -\frac{1}{2\omega} \left(\frac{1}{2}(\xi_1 + \xi_2)\omega a_2 - \kappa a_1 \sin(\theta_1 - \theta_2) + \frac{1}{2}(\xi_1 - \xi_2)\omega a_1 \cos(\theta_1 - \theta_2) \right), \quad (7)$$

$$\dot{\theta}_2 = -\frac{1}{2a_2\omega} \left(\omega^2 a_2 + \frac{1}{2}(\xi_1 - \xi_2)\omega a_1 \sin(\theta_1 - \theta_2) - a_2 - \kappa a_2 + \kappa a_1 \cos(\theta_1 - \theta_2) \right), \quad (8)$$

in terms of the unknowns $a_1, a_2, \theta_1, \theta_2$ and their associated time derivatives. Without loss of generality, the amplitudes are defined as positive $a_1 > 0, a_2 > 0$. The terms $k_{\text{eq}}(a_1)$ and $d_{\text{eq}}(a_1)$ are the equivalent stiffness and damping of the Jenkins element as defined later.

Without loss of generality, one can reduce the problem to an autonomous set of 3 equations governing that (slow) amplitude modulations a_1 and a_2 and the (slow) phase difference (lag) which is defined as $\Delta\theta = \theta_1 - \theta_2$. This leads to what we will refer to as *slow flow equations*,

$$\dot{a}_1 = -\frac{1}{2\omega} \left(\kappa a_2 \sin(\Delta\theta) + \frac{1}{2}(\xi_1 - \xi_2)\omega a_2 \cos(\Delta\theta) + \frac{1}{2}(\xi_1 + \xi_2)\omega a_1 + \gamma \omega d_{\text{eq}}(a_1) a_1 \right), \quad (9)$$

$$\dot{a}_2 = -\frac{1}{2\omega} \left(\frac{1}{2}(\xi_1 + \xi_2)\omega a_2 - \kappa a_1 \sin(\Delta\theta) + \frac{1}{2}(\xi_1 - \xi_2)\omega a_1 \cos(\Delta\theta) \right), \quad (10)$$

$$\Delta\dot{\theta} = \frac{1}{2\omega} \left(-\gamma + \gamma k_{\text{eq}}(a_1) + \kappa \cos(\Delta\theta) \left(\frac{a_1}{a_2} - \frac{a_2}{a_1} \right) + \frac{1}{2}(\xi_1 - \xi_2)\omega \sin(\Delta\theta) \left(\frac{a_1}{a_2} + \frac{a_2}{a_1} \right) \right). \quad (11)$$

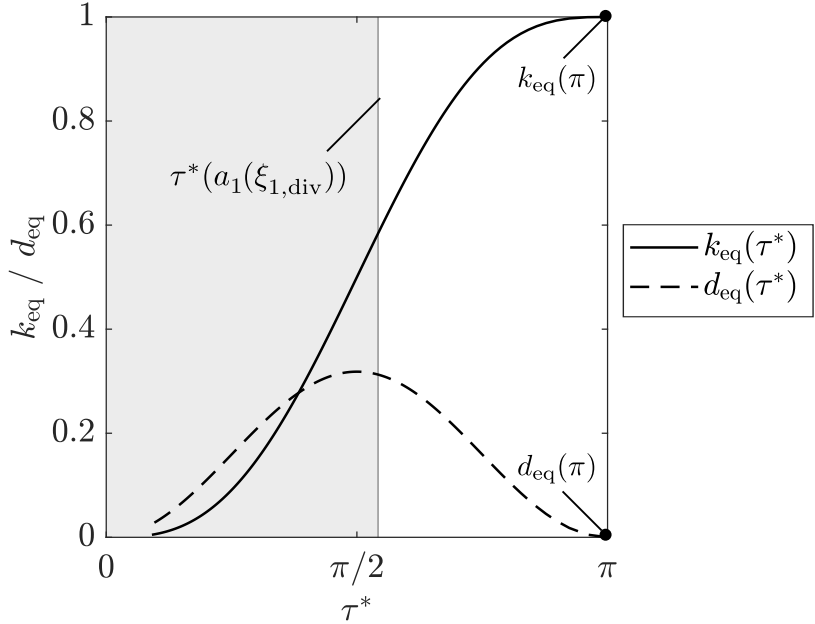


Figure 3: Behavior of k_{eq} and d_{eq} with respect to τ^* ; point of divergence $\xi_{1,\text{div}}$ determined by numerical simulation of Eq. (1)-(2) with $\xi_1 < 0$, $\xi_2 = 0.011$, $\kappa = 0.1$, $\gamma = 0.5$

Averaging the nonlinear force of the Jenkins element, $f_t[x_1]$, yields the expressions for the amplitude-dependent equivalent stiffness k_{eq} and damping d_{eq} [7] as follows:

$$k_{\text{eq}}(a_1) = \frac{2\tau^*(a_1) - \sin(2\tau^*(a_1))}{2\pi}, \quad \omega d_{\text{eq}}(a_1) = \frac{1}{\pi} \sin^2(\tau^*(a_1)) \quad (12)$$

$$\text{with } \tau^*(a_1) = \begin{cases} \arccos(1 - \frac{2}{a_1}) & a_1 > 1 \\ \pi & 0 < a_1 \leq 1 \end{cases}. \quad (13)$$

In the sticking case it holds that, $a_1 \leq 1$, and the Jenkins element correctly degenerates to a conservative spring with $k_{\text{eq}} = 1$ and $d_{\text{eq}} = 0$. In addition, the equivalent damping reaches a maximum for $\tau^* = \pi/2$, where $k_{\text{eq}} = 0.5$. As the amplitude goes to infinity, the friction effect becomes negligible such that both k_{eq} and d_{eq} asymptotically approach zero. The nonlinear dependence of the equivalent damping and stiffness with respect to the parameter τ^* is depicted in Fig. 3.

3.2. Approximation of the energy-dependent oscillation frequency

To simulate the slow flow given by Eqs. (9)-(11), the oscillation frequency ω needs to be specified. We are interested in the dynamics near the LCO. Indeed, to compute the LCO with frequency ω , we impose conditions for periodicity, namely, $\dot{a}_1 = \dot{a}_2 = \dot{\theta}_1 = \dot{\theta}_2 = 0$. With this, Eqs. (5)-(8) degenerate to an algebraic system of four equations for the four unknowns a_1 , a_2 , $\Delta\theta$ and ω , which are solved numerically. The resulting frequency of the LCO is illustrated in Fig. 4, where it is depicted as function of the corresponding mechanical energy of the system when it oscillates on the LCO, obtained by varying the negative damping $\xi_1 < 0$. This frequency-energy relation holds strictly only at the LCO, i.e., for the time-periodic solution, which represents a special stationary solution of the mechanical system with negative damping. Perturbing the initial conditions corresponding to the LCO, but staying sufficiently close in the neighborhood of the LCO, we postulate that this frequency-energy relation still provides a reasonable approximation denoted symbolically in the form,

$$\omega = \tilde{\omega}(E_{\text{mech}}(a_1, a_2, \Delta\theta)). \quad (14)$$

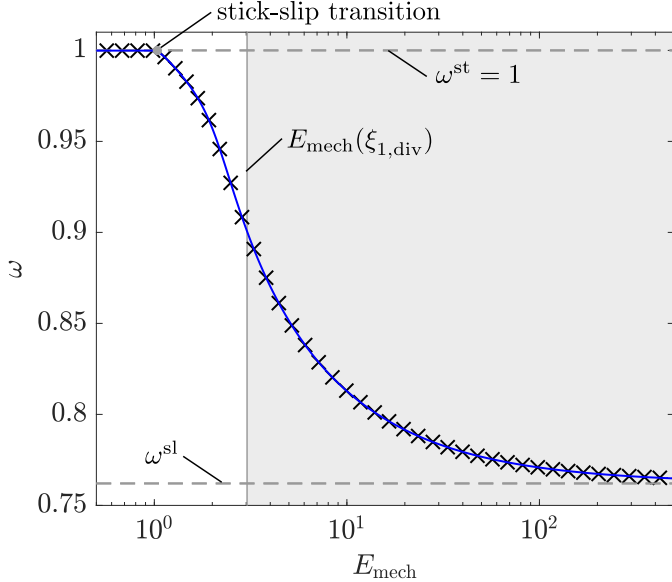


Figure 4: Frequency-energy relation along the LCO obtained under variation of $\xi_1 < 0$: The discrete points ('black','x') are obtained by solving the slow flow equations Eq. (9)-(11) ($\dot{a}_1 = \dot{a}_2 = \Delta\dot{\theta} = 0$), initialized with small/high mechanical energy for solutions along the lower/upper half of the LCO curve (cf. Fig. 1), or, continuous interpolation of the discrete solution points by piecewise cubic splines ('blue', 'solid'); indication of limit cases for sticking slider ω_{st} and frictionless sliding ω_{sl} ; point of divergence $\xi_{1,\text{div}}$ determined by numerical simulation of Eq. (1)-(2); $\xi_1 < 0$, $\xi_2 = 0.011$, $\kappa = 0.1$, $\gamma = 0.5$

Of course, the above described numerical solution method only generates a discrete sequence of points. To simulate the slow flow Eqs. (9)-(11), however, a continuous expression (i. e., a function) of the oscillation frequency in terms of the states $a_1, a_2, \Delta\theta$ is needed, which we obtained using interpolation. To this end, we applied a piecewise cubic spline interpolation between about 400 discrete solution points in the interval $E_{\text{mech}} \in (0, 500)$. Note, that this interval contains also energy levels beyond the fold bifurcation (i. e., points along the upper half of the LCO curve), cf. Fig. 1.

3.3. Cascade of period-doubling leads to chaos

Now, we are in the position to analyze to what extent the slow flow approximation, Eqs. (5)-(8) together with Eq. (14), reproduces the dynamics of the initial system, Eqs. (1)-(2). We note at this point that the ansatz used for the previous Complexification-Averaging analysis, is based on the assumption that there exists a single fast frequency ω , and that there is a slow-fast separation of the non-stationary dynamics, i. e., that there is no mixing of scales. Whenever either of these conditions is not satisfied we expect that our analytical predictions will diverge compared to the exact solutions derived by direct numerical simulations of the initial system of governing equations. In Fig. 5, we compare the bifurcation diagrams, with respect to the negative damping parameter ξ_1 . The vibration level is depicted in terms of the maximum, $a_{1,\text{max}}$, and minimum, $a_{1,\text{min}}$, vibration amplitudes at steady state; we note that the derived steady-state is not necessarily periodic, nor even stationary. Given the complexity of the non-stationary dynamics of the system, both the secondary Hopf bifurcation point, $\xi_{1,\text{Hopf}}$, and the point of divergence, $\xi_{1,\text{div}}$, are captured by the analysis with remarkable accuracy. The minor deviations are attributed to the aforementioned analytical simplifications: Truncation to a single harmonic, separation of time scales and presumed invariance of frequency-energy dependence.

Fig. 6 depicts Poincaré maps associated with a Poincaré section \mathcal{S} (associated with the *fast time scale*). To this end, given that the initial system Eqs. (1)-(2) is four-dimensional, and hamiltonian, we introduce the following two-dimensional Poincaré (cut) section,

$$\mathcal{S} = \{\mathbf{x} | x_2 = 0, \dot{x}_2 > 0\} \quad (15)$$

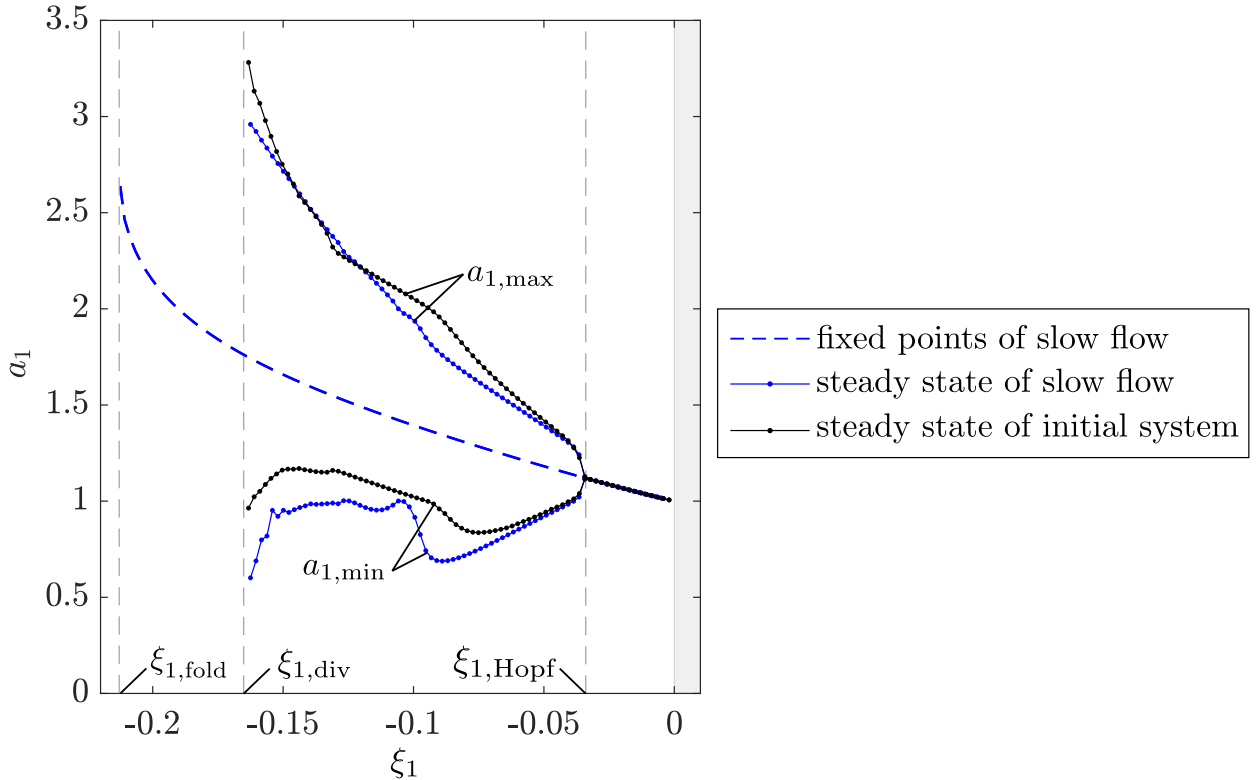


Figure 5: Comparison of the slow flow approximation (Eqs. (9)-(11)) against the initial system (Eqs. (1)-(2)) with respect to the amplitude-damping diagram: The discrete points are obtained by direct numerical integration initialized on the LCO considering a small perturbation; $\xi_1 < 0$, $\xi_2 = 0.011$, $\kappa = 0.1$, $\gamma = 0.5$

with respect to the initial, fast variables $\mathbf{x} = [x_1, x_2, \dot{x}_1, \dot{x}_2]^T$. Studying the intersections of the orbits of the dynamical system with the Poincaré section \mathcal{S} we obtain a two-dimensional projection of the three-dimensional Poincaré map. It can be seen that the LTO transitions towards chaotic oscillations for increasing magnitude of the negative damping. The corresponding analytical predictions obtained from the slow flow approximation are depicted in Fig. 7. Here, the evolution of the variables \mathbf{x} on the fast time scale was recovered using Eq. (4). Again, the slow flow approximation is in good agreement with the exact numerical simulation. We conclude that the proposed slow flow approximation, including the assumptions on the frequency-energy dependence, is sufficiently accurate to further characterize the dynamics on the slow time scale.

Fig. 8 depicts Poincaré maps associated with a different Poincaré section \mathcal{D} for the slow flow dynamics Eqs. (9)-(11),

$$\mathcal{D} = \{\mathbf{a} | \underline{a}_2 = 0, \dot{\underline{a}}_2 > 0\} \quad (16)$$

with respect to the slow variables $\mathbf{a} = [\underline{a}_1, \underline{a}_2, \dot{\underline{a}}_1, \dot{\underline{a}}_2]^T$. Here, \square denotes mean-free variables. Note that the amplitudes a_1 and a_2 typically do not have zero crossings. Hence, the steady-state mean value is subtracted so that one can use the common formulation of the Poincaré section in Eq. (16) (involving zero crossings). The slow time scale provides a clearer picture of the dynamics: The (quasi-periodic) limit torus oscillations are seen as closed curves in the phase projections within Fig. 8. The Poincaré map consists of a single point for $\xi_1 = -0.055$. Apparently, a cascade of period doubling bifurcations takes place until the chaotic regime is reached. In [5], the chaotic nature of the dynamics past the secondary Hopf bifurcation was confirmed by numerically computed Lyapunov exponents.

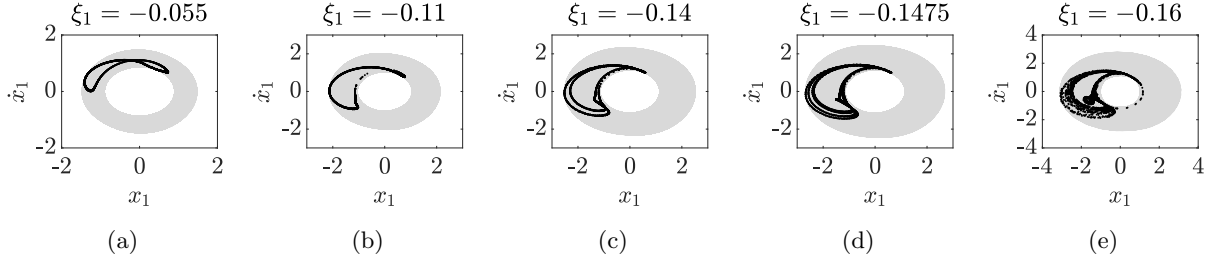


Figure 6: Phase space projection ('grey', 'solid') and Poincaré map ('black', '.') associated with section \mathcal{S} (associated with the *fast time scale*), obtained by direct numerical simulations of the initial system Eqs. (1)-(2).

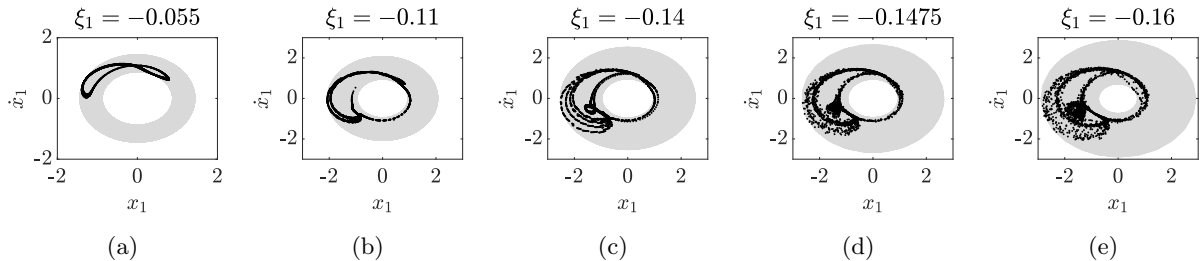


Figure 7: Phase space projection ('grey', 'solid') and Poincaré map ('black', '.') associated with section \mathcal{S} (associated with the *fast time scale*), obtained from the analytical slow flow approximation.

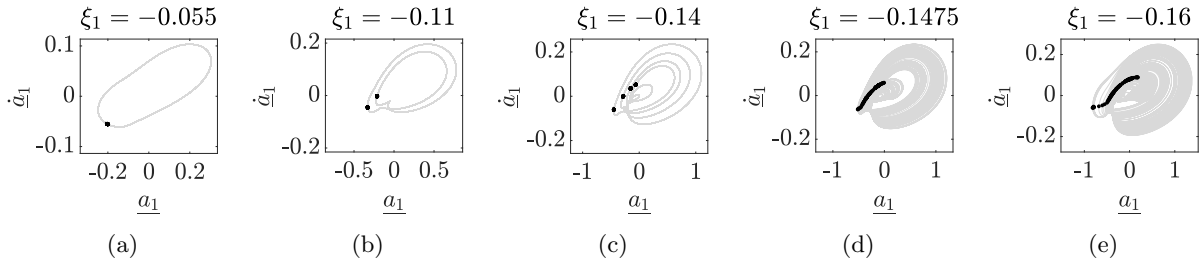


Figure 8: Phase space projection ('grey', 'solid') and Poincaré map ('black', '.') associated with \mathcal{D} (associated with the *slow time scale*), obtained from the slow flow approximation; \square represents mean-free variables.

4. Analytical investigation of the secondary Hopf bifurcation

We now focus on the transition from limit cycle oscillations to limit torus oscillations. We seek to establish analytically the conditions for the emergence of non-periodic, non-stationary oscillations in the mechanical system of Fig. 2, and to obtain a closed-form approximation for the point of the secondary Hopf bifurcation. To this end, we use perturbation calculus to approximate the family of LCOs and analyze its stability. The accuracy and efficacy of the analytical methodology is evaluated by comparison against the exact numerical simulation of the initial problem Eqs. (1)-(2).

4.1. Approximation of the fixed points of the slow flow by means of perturbation analysis

The LCO (time periodic solution) on the fast time scale corresponds to a fixed point of the slow flow, and is determined by setting the left hand sides of Eqs. (5)-(8) to zero. It turned out to be useful to transform the slow flow by introducing a new set of variables: Instead of a_1, a_2 we introduce the new variables $\rho = a_2/a_1$ and τ^* (stick-slip transition time) which is uniquely related to a_1 as defined in Eq. (13). With this variable transformation, the governing algebraic equations determining the fixed points of the slow flow can be cast

into the form:

$$0 = \kappa \hat{\rho} \sin(\Delta\hat{\theta}) + \frac{1}{2}(\xi_1 - \xi_2) \hat{\omega} \hat{\rho} \cos(\Delta\hat{\theta}) + \frac{1}{2}(\xi_1 + \xi_2) \hat{\omega} + \gamma \hat{\omega} d_{\text{eq}}(\hat{\tau}^*), \quad (17)$$

$$0 = \kappa \hat{\rho} \cos(\Delta\hat{\theta}) - \frac{1}{2}(\xi_1 - \xi_2) \hat{\omega} \sin(\Delta\hat{\theta}) \hat{\rho} + \hat{\omega}^2 - \kappa + \gamma - \gamma k_{\text{eq}}(\hat{\tau}^*) - 1 \quad (18)$$

$$0 = \frac{1}{2}(\xi_1 + \xi_2) \hat{\omega} \hat{\rho} - \kappa \sin(\Delta\hat{\theta}) + \frac{1}{2}(\xi_1 - \xi_2) \hat{\omega} \cos(\Delta\hat{\theta}), \quad (19)$$

$$0 = \hat{\omega}^2 + \frac{1}{2}(\xi_1 - \xi_2) \hat{\omega} \sin(\Delta\hat{\theta}) \hat{\rho}^{-1} - 1 - \kappa + \kappa \hat{\rho}^{-1} \cos(\Delta\hat{\theta}). \quad (20)$$

We use perturbation calculus to approximate the fixed points of this set of transformed system of algebraic equations. To this end, we introduce the small parameter ε which will act as the formal perturbation parameter of our analysis. To introduce the small parameter we assume that the coupling and damping terms are small, scaled according to the following relations:

$$\kappa = \varepsilon \bar{\kappa}, \quad \xi_1 = \varepsilon^2 \bar{\xi}_1, \quad \xi_2 = \varepsilon^2 \bar{\xi}_2. \quad (21)$$

Recall that the condition of weak coupling is needed to have closely-spaced natural frequencies in the mechanical system of Fig. 2: The ratio of the natural frequencies in the linear case when sticking contact occurs equals $\sqrt{1+2\kappa}$. A typical value for κ is 0.1 leading to about 10% difference in the natural frequencies. Moreover, the secondary Hopf bifurcation occurs already for very light damping, with typical values for ξ_1 in the range -0.035 for ξ_2 of 0.011 . Thus, it holds that $\|\xi_{1,2}\| \ll \kappa \ll 1$, as defined in Eq. (21). It should be emphasized that *nonlinearity is not assumed as weak*, i.e., γ is considered to be a system parameter of order $\mathcal{O}(\varepsilon^0)$. Yet we impose the condition $\gamma \leq 1$ which is necessary to have positive stiffness values for all springs in the model (Fig. 2).

We seek an approximation to the fixed point in terms of $\hat{\tau}^*$, $\hat{\rho}$, $\Delta\hat{\theta}$ and $\hat{\omega}$, where $\hat{\square}$ denotes fixed point quantities. In accordance with regular perturbation theory (see e.g., [6]), these quantities are expanded in regular power series in ε , of the form

$$f = f_0 + f_1 \varepsilon + f_2 \varepsilon^2 + \mathcal{O}(\varepsilon^3). \quad (22)$$

As will be shown later, reasonable results are achieved already for a second-order approximation (up to and including the ε^2 term). The power series and Eq. (21) are substituted into Eqs. (17)-(20). The equations contain several nonlinear terms, namely, $\sin(\Delta\hat{\theta})$, $\cos(\Delta\hat{\theta})$, $\omega d_{\text{eq}}(\hat{\tau}^*)$, $k_{\text{eq}}(\hat{\tau}^*)$, and $1/\rho$. In accordance with perturbation calculus, each nonlinear term is expanded into a Taylor series of sufficient order, and the power series of the unknowns (Eq. (22)) is substituted. The unknown coefficients of the power series are then determined successively by matching (balancing) the coefficients at each order separately, starting with the leading-order $\mathcal{O}(\varepsilon^0)$ terms. With this, the following second-order approximation of the fixed point of the slow flow equations is obtained:

$$\hat{\tau}^* = \pi - \sqrt{\frac{-2\pi \bar{\xi}_1}{\gamma}} \varepsilon + \mathcal{O}(\varepsilon^3), \quad (23)$$

$$\hat{\rho} = 1 + \left(\frac{\bar{\xi}_1^2}{\bar{\kappa}^2} - \frac{\bar{\xi}_1 \bar{\xi}_2}{2 \bar{\kappa}^2} - \frac{4}{3\bar{\kappa}} \sqrt{\frac{-2\bar{\xi}_1^3 \pi}{\gamma}} \right) \varepsilon^2 + \mathcal{O}(\varepsilon^3), \quad (24)$$

$$\Delta\hat{\theta} = \frac{\bar{\xi}_1}{\bar{\kappa}} \varepsilon + \mathcal{O}(\varepsilon^3), \quad (25)$$

$$\hat{\omega} = 1 + \mathcal{O}(\varepsilon^3). \quad (26)$$

As expected, non-trivial fixed points only exists for $\xi_1 \leq 0$.

4.2. Calculation of the secondary Hopf bifurcation point

Clearly, the limit torus on the fast time scale corresponds to a periodic orbit on the slow time scale, and the bifurcation of the limit cycle to the limit torus corresponds to a secondary Hopf bifurcation. Consequently, on the slow time scale, this point is associated with (primary) Hopf bifurcation of the fixed point of the slow flow equations given by Eqs. (23)-(26). Hence, to locate this point and establish conditions for its existence, it suffices to analyze the asymptotic stability of the approximated fixed point of the slow flow and prove that the conditions for Hopf bifurcation hold at the point of instability of the fixed point. This is done in the conventional way, based on the eigenvalues of the Jacobian with respect to the slow flow Eqs. (9)-(11). Accordingly, the characteristic equation governing the eigenvalues, λ , can be explicitly computed by imposing the following condition,

$$\frac{1}{2} \begin{vmatrix} -j_1 - d_1 - \lambda & -d_2 c - \bar{\kappa} s & -\bar{\kappa} \hat{\rho} c + \hat{\rho} d_2 s \\ -d_2 c + \bar{\kappa} s & -d_1 - \lambda & \bar{\kappa} c + d_2 s \\ \bar{\kappa} (\hat{\rho} + \hat{\rho}^{-1}) c - d_2 (\hat{\rho} - \hat{\rho}^{-1}) s + j_2 & -\bar{\kappa} (1 + \hat{\rho}^{-2}) c + d_2 (1 - \hat{\rho}^{-2}) s & d_2 (\hat{\rho} + \hat{\rho}^{-1}) c + \bar{\kappa} (\hat{\rho} - \hat{\rho}^{-1}) s - \lambda \end{vmatrix} = 0,$$

where the following abbreviations have been introduced, $d_1 = \frac{1}{2} (\bar{\xi}_1 + \bar{\xi}_2)$, $d_2 = \frac{1}{2} (\bar{\xi}_1 - \bar{\xi}_2)$, $s = \sin(\Delta\hat{\theta})$ and $c = \cos(\Delta\hat{\theta})$, together with the additional notations,

$$j_1 = \gamma \frac{\partial a_1 d_{\text{eq}}(a_1)}{\partial a_1} \Big|_{a_1=\hat{a}_1} = \gamma \frac{(\cos(\hat{\tau}^*) - 1)^2}{\pi} = \frac{4\gamma}{\pi} + 4\bar{\xi}_1 \varepsilon^2 + \mathcal{O}(\varepsilon^3),$$

$$j_2 = \gamma a_1 \frac{\partial k_{\text{eq}}(a_1)}{\partial a_1} \Big|_{a_1=\hat{a}_1} = -\gamma \frac{2(\cos(\hat{\tau}^*) - 1)(\cos(\hat{\tau}^*)^2 - 1)}{\pi \sin(\hat{\tau}^*)} = 4\sqrt{\frac{-2\gamma\bar{\xi}_1}{\pi}} \varepsilon + \mathcal{O}(\varepsilon^3).$$

The solution of the characteristic equation yields the following second-order analytical approximation for the eigenvalues:

$$\lambda^{(1)} = -\frac{2\gamma}{\pi} - \frac{\left((9\bar{\xi}_1 + \bar{\xi}_2)\gamma - \pi\bar{\kappa}^2 - 2\bar{\kappa}\sqrt{-2\pi\gamma\bar{\xi}_1}\right)}{4\gamma} \varepsilon^2 + \mathcal{O}(\varepsilon^3), \quad (27)$$

$$\lambda^{(2,3)} = \pm i \frac{\sqrt{2}}{2} \bar{\kappa} \varepsilon - \frac{-(\bar{\xi}_1 - 3\bar{\xi}_2)\gamma + \pi\bar{\kappa}^2 + 2\bar{\kappa}\sqrt{-2\pi\gamma\bar{\xi}_1}}{8\gamma} \varepsilon^2 + \mathcal{O}(\varepsilon^3). \quad (28)$$

Recalling that $\xi_1 < 0$, one can infer that $\lambda^{(1)}$ remains real-valued, whereas $\lambda^{(2,3)}$ appear as a complex-valued pair. Thus, the sought bifurcation occurs when $\lambda^{(2,3)}$ crosses the imaginary axis. This is the necessary condition for the realization of the Hopf bifurcation; it can also be shown (not reported here) that the additional sufficient conditions are also met [8]. So indeed a Hopf bifurcation occurs at the point of instability of the fixed point and a new limit cycle oscillation is generated in the slow flow dynamics (which corresponds to the limit torus oscillation in the fast dynamics).

The condition $\Re\{\lambda^{(2,3)}\} = 0$ leads to the following value for the critical damping,

$$\xi_{1,\text{Hopf}}^{\text{start/end}} = 3\xi_2 \left(1 - \nu \left(1 \mp \frac{2\sqrt{2}}{3} \sqrt{1 - \frac{3}{\nu}}\right)\right) \quad (29)$$

$$\text{with } \nu = \frac{\pi\kappa^2}{\gamma\xi_2}. \quad (30)$$

Apparently, besides the expected transition from limit cycle to limit torus, another transition back to a stable cycle is possible. This will be further discussed in the next subsection. It is interesting to note that the bifurcation value $\xi_{1,\text{Hopf}}^{\text{start/end}}$ is a function of the out-of-phase damping ξ_2 and the coupling-to-nonlinearity-ratio κ^2/γ . This relation is illustrated in Fig. 9(a). Solutions for $\xi_{1,\text{Hopf}}^{\text{start/end}}$ only exist for $\nu \geq 3$, i.e. if $\frac{\kappa^2}{\gamma} \geq \frac{3\xi_2}{\pi}$. This means that the positive damping of the (out-of-phase) higher-frequency mode must be sufficiently small (for given γ and κ) for this bifurcation to occur.

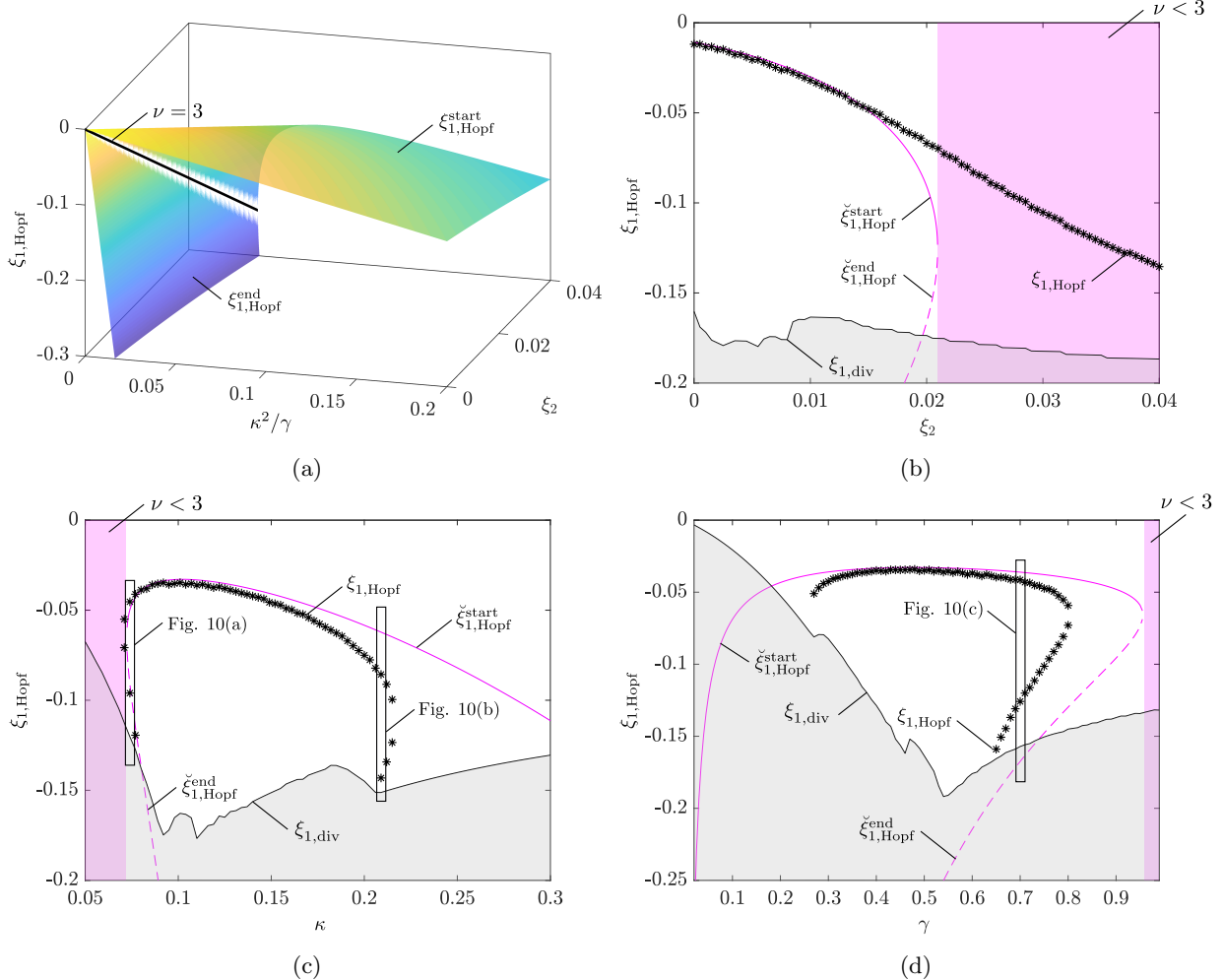


Figure 9: Critical damping $\xi_{1,\text{Hopf}}$ at the secondary Hopf bifurcation: (a) Dependence of analytical result on out-of-phase damping ξ_2 and coupling-to-nonlinearity ratio κ^2/γ ; (b)-(d) comparison of the analytical result ('pink') to exact result determined by direct numerical simulation of the original equations of motion Eqs. (1)-(2) ('black') under variation of ξ_2 , κ and γ . Nominal parameters are set to $\xi_2 = 0.011$, $\kappa = 0.1$, $\gamma = 0.5$.

4.3. Assessment of the analytical results against the exact numerical simulations

We now compare the previous analytical results to the results of exact numerical simulations. The location of the secondary Hopf bifurcation, in terms of the critical damping value $\xi_{1,\text{Hopf}}$, is illustrated in Fig. 9. The corresponding analytical result is given in Eq. (29). As throughout this work, the numerical reference was obtained by simulation of the initial system, Eqs. (1)-(2).

Overall the analytical result is in good agreement with the numerical reference. Deviations occur at the ranges where the assumptions underlying the perturbation approach are violated. More specifically, the assumption concerning the hierarchy of the orders of magnitude, $\|\xi_{1,2}\| \ll \kappa \ll \gamma$ (cf. Eq. (21)) must hold to ensure reasonable accuracy. For instance, the analytical results are accurate for $\xi_2 < 0.02$ (Fig. 9b) and $\xi_2 < \kappa < 0.2$ (Fig. 9c). In contrast, if $\|\xi_1\|$ or ξ_2 approach the order of κ , the accuracy is poor (as expected). Similarly, if κ approaches the order of γ (order ε^0), the analytical result is no longer valid.

As noted earlier, the analytical approximation yields two critical values of ξ_1 , as expressed in Eq. (29). The one with smaller magnitude, $\xi_{1,\text{Hopf}}^{\text{start}}$, corresponds to the point where the limit cycle becomes unstable giving rise to a stable limit torus. The one with larger magnitude, $\xi_{1,\text{Hopf}}^{\text{end}}$, refers to another secondary Hopf

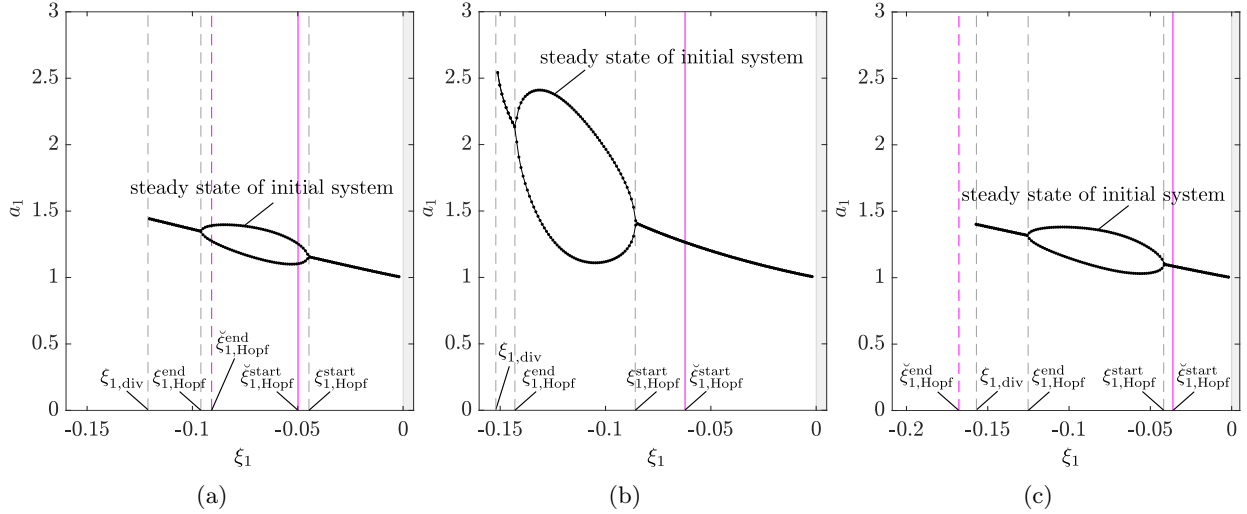


Figure 10: Examples for which the limit cycle regains stability via another secondary Hopf bifurcation: (a) $\kappa = 0.074, \xi_2 = 0.011, \gamma = 0.5$, (b) $\kappa = 0.21, \xi_2 = 0.011, \gamma = 0.5$, (c) $\gamma = 0.7, \kappa = 0.1, \xi_2 = 0.011$. Analytical result in 'pink', numerical reference in 'black'. The parameter sets are indicated in Fig. 9.

bifurcation where the limit cycle regains stability. As seen from these results, for a wide range of parameters, $\check{\xi}_{1,\text{Hopf}}^{\text{end}}$ lies beyond the point of divergence, $\xi_{1,\text{div}}$, and, therefore, it is never reached. For other parameter combinations, however, the secondary Hopf bifurcation can be reached, e.g. for $0.6 < \gamma < 0.8$ in Fig. 9(d), or for $\kappa \approx 0.074$ and $\kappa \approx 0.21$ in Fig. 9(c). The resulting bifurcation diagram is illustrated in Fig. 10 for three different parameter sets. Again, reasonable agreement between the analytical results and numerical solutions is achieved with respect to the bifurcation point.

5. Conclusions

We considered a system of two weakly coupled oscillators, with an elastic dry friction element attached to one of the oscillators, subjected to negative viscous damping of the symmetric in-phase and positive damping of the out-of-phase motion. When increasing the magnitude of the negative damping, the well-understood limit cycle oscillations lose stability and bifurcate into limit torus oscillations. For some parameter ranges, an additional secondary Hopf bifurcation may occur beyond which the limit cycle regains stability. In other cases, the quasi-periodic oscillations further bifurcate into chaotic dynamics. The analysis of the slow flow in the neighborhood of the limit cycle revealed that chaos is reached via a cascade of period doubling bifurcations. Assuming weak coupling, of $\mathcal{O}(\varepsilon)$, (leading to closely-spaced natural frequencies) and even weaker damping, of $\mathcal{O}(\varepsilon^2)$, we derived an analytical approximation of the limit cycle using perturbation calculus. A stability analysis provided a closed-form expression for the point of the secondary Hopf bifurcation and conditions for its existence. In particular, it was established that non-periodic oscillations occur for sufficiently weak coupling and sufficiently strong nonlinearity. The quality of the analytical results was thoroughly validated by comparing them against exact numerical simulations of the original equations of motion of the initial dynamical system.

The key challenge for deriving the closed-form approximations was the treatment of the dry friction non-linearity (Jenkins element). To tackle this, a change of variables was carried out, involving the normalized stick-slip transition time. As the Jenkins element is commonly used to model nonlinear hysteresis (including tribology and material behavior) we believe that the proposed approach will be instrumental to analyze systems far beyond the one considered in this work. Here, we anticipate that our results will trigger more efforts within our scientific community to derive analytical approximations in order to gain deep understanding of parameter dependencies, in addition to systematic numerical simulation. This will help in predictive design of oscillating systems with dry friction undergoing instabilities, LCOs, LTOs and chaotic motions.

Acknowledgement

The author Alexander F. Vakakis would like to acknowledge the support of a von Humboldt Award which made possible his visit at the University of Stuttgart.

Declarations

Funding No funding was received for conducting this study.

Conflicts of interest The authors declare that they have no conflict of interest.

Availability of data and material The datasets generated during the current study are available from the corresponding author on reasonable request.

Code availability The codes generated during the current study are available from the corresponding author on reasonable request.

Authors' contributions (optional)

References

- [1] M. R. Brake, The Mechanics of Jointed Structures, Springer International Publishing, Cham, 2018. doi:10.1007/978-3-319-56818-8.
- [2] M. Krack, L. Salles, F. Thouverez, Vibration prediction of bladed disks coupled by friction joints, *Archives of Computational Methods in Engineering* 24 (3) (2017) 589–636. doi:10.1007/s11831-016-9183-2.
- [3] A. Sinha, J. H. Griffin, Friction damping of flutter in gas turbine engine airfoils, *Journal of Aircraft* 20 (4) (1983) 372–376. doi:10.2514/3.44878.
- [4] A. Sinha, J. H. Griffin, Effects of friction dampers on aerodynamically unstable rotor stages, *AIAA Journal* 23 (2) (1985) 262–270. doi:10.2514/3.8904.
- [5] L. Woiwode, J. Gross, M. Krack, Effect of modal interactions on friction-damped self-excited vibrations, *Journal of Vibration and Acoustics* 143 (3) (2021) 545. doi:10.1115/1.4048396.
- [6] A. F. Vakakis, L. A. Bergman, O. V. Gendelman, G. M. L. Gladwell, G. Kerschen, Y. S. Lee, D. M. McFarland (Eds.), Nonlinear Targeted Energy Transfer in Mechanical and Structural Systems, Vol. 156 of Solid Mechanics and Its Applications, Springer Netherlands, Dordrecht, 2009. doi:10.1007/978-1-4020-9130-8.
URL <http://site.ebrary.com/lib/alltitles/docDetail.action?docID=10271960>
- [7] J. H. Griffin, Friction damping of resonant stresses in gas turbine engine airfoils, *Journal of Engineering for Power* 102 (2) (1980) 329–333. doi:10.1115/1.3230256.
- [8] J. Guckenheimer, P. Holmes, Nonlinear Oscillations, Dynamical Systems, and Bifurcations of Vector Fields, Vol. 42, Springer New York, New York, NY, 1983. doi:10.1007/978-1-4612-1140-2.

Figures

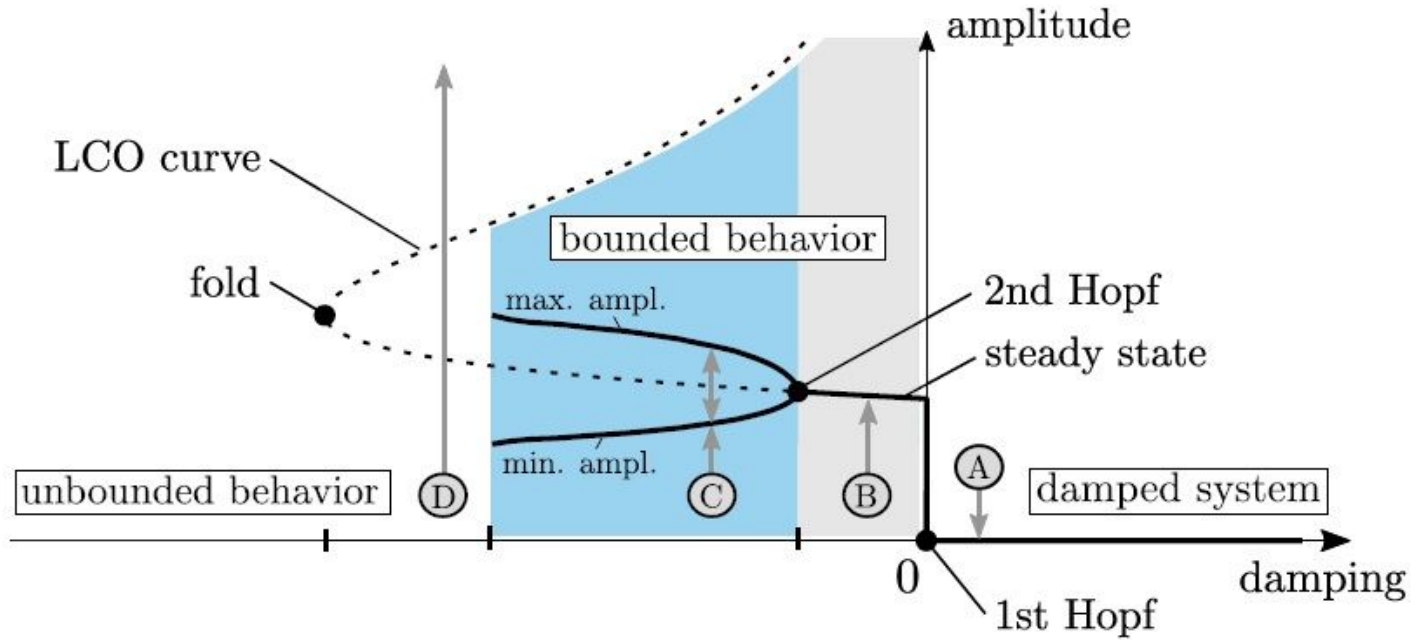


Figure 1

(see Manuscript file for figure legend)

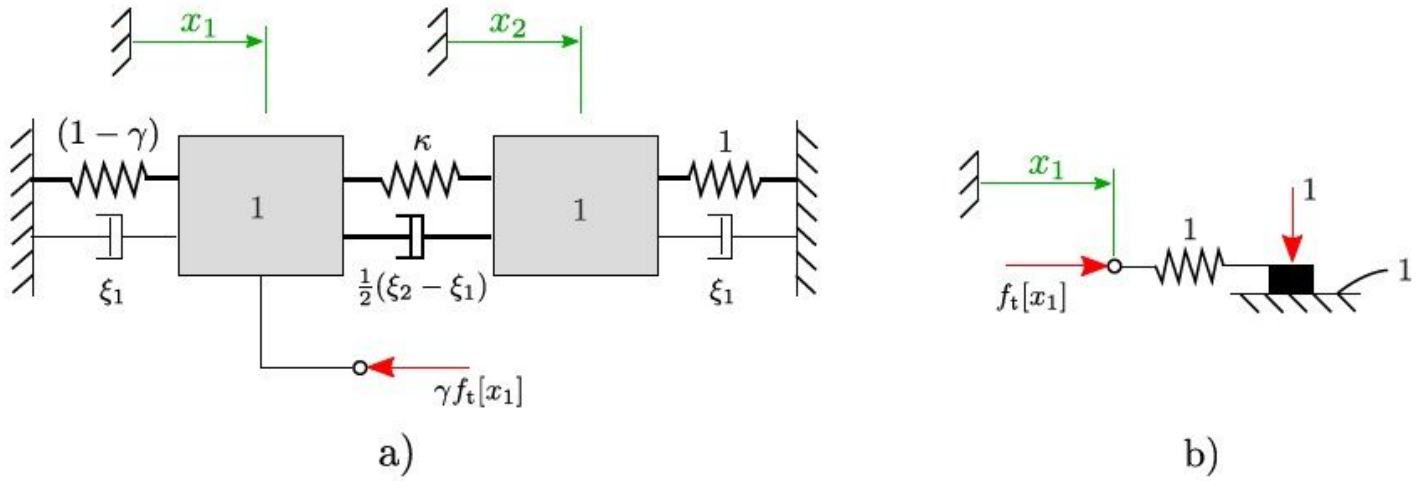


Figure 2

(see Manuscript file for figure legend)

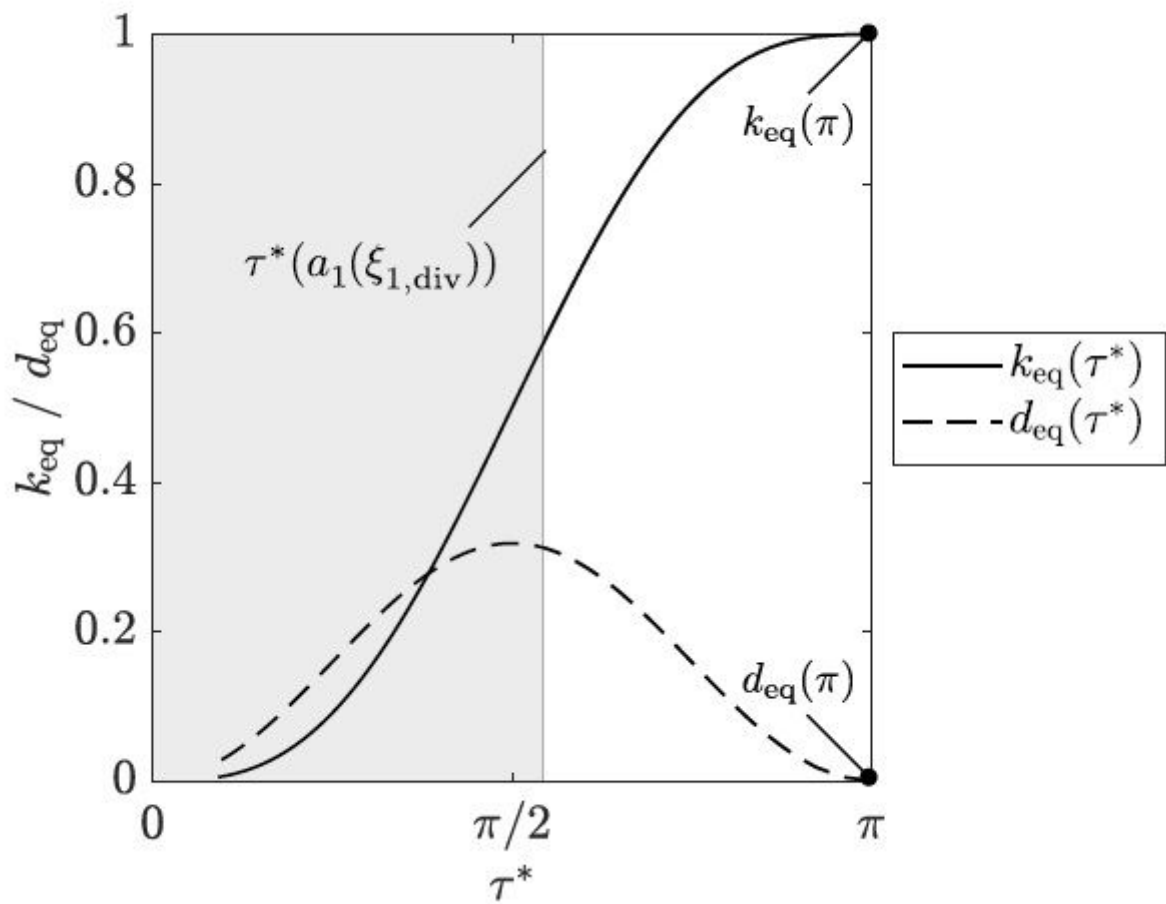


Figure 3

(see Manuscript file for figure legend)

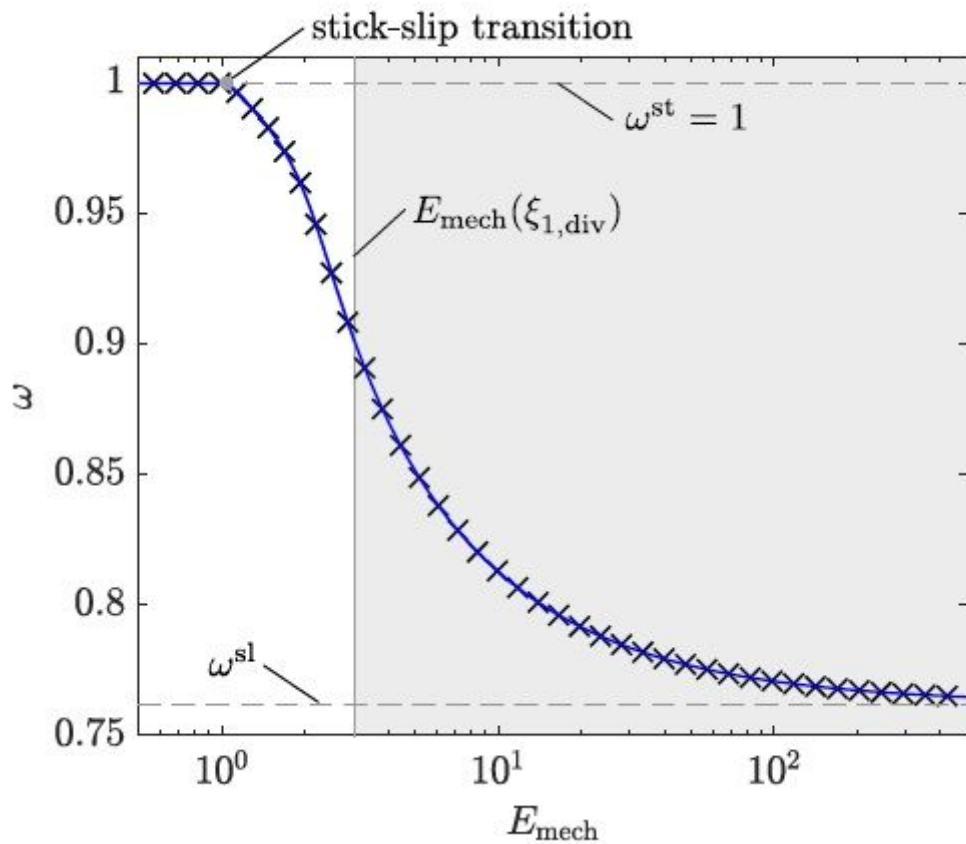


Figure 4

(see Manuscript file for figure legend)

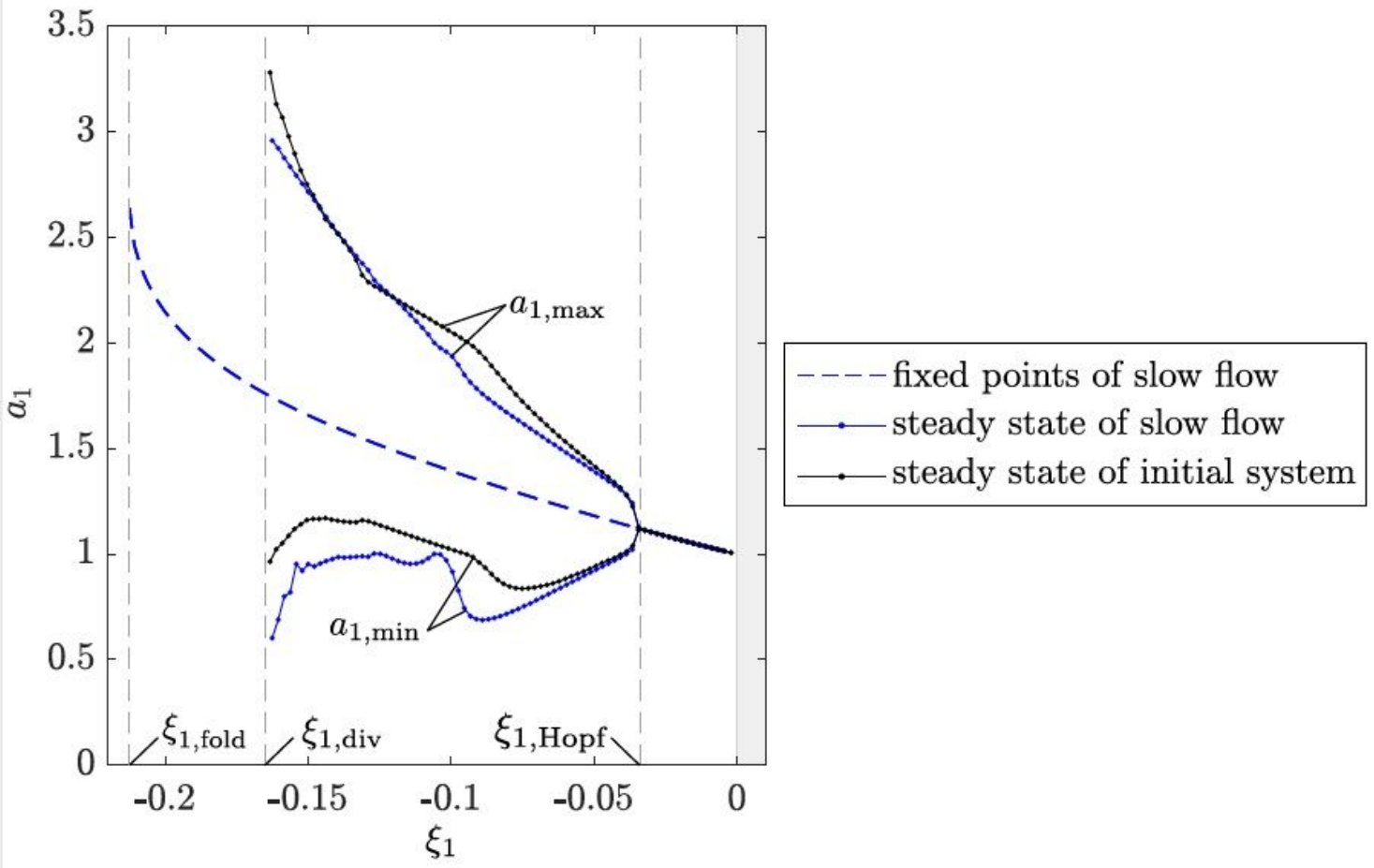


Figure 5

(see Manuscript file for figure legend)

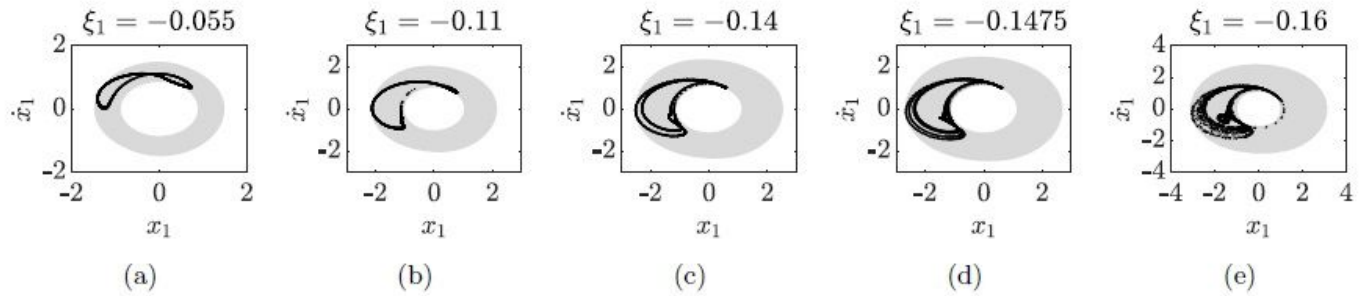


Figure 6

(see Manuscript file for figure legend)

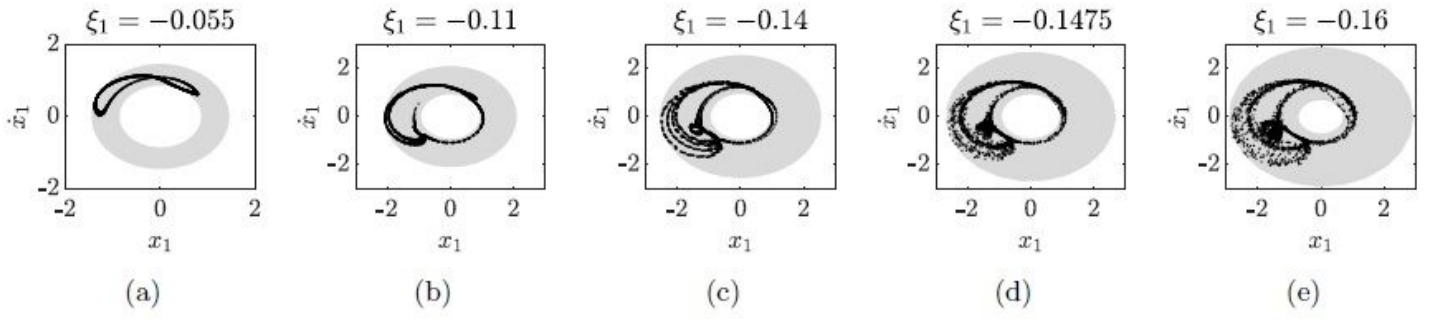


Figure 7

(see Manuscript file for figure legend)

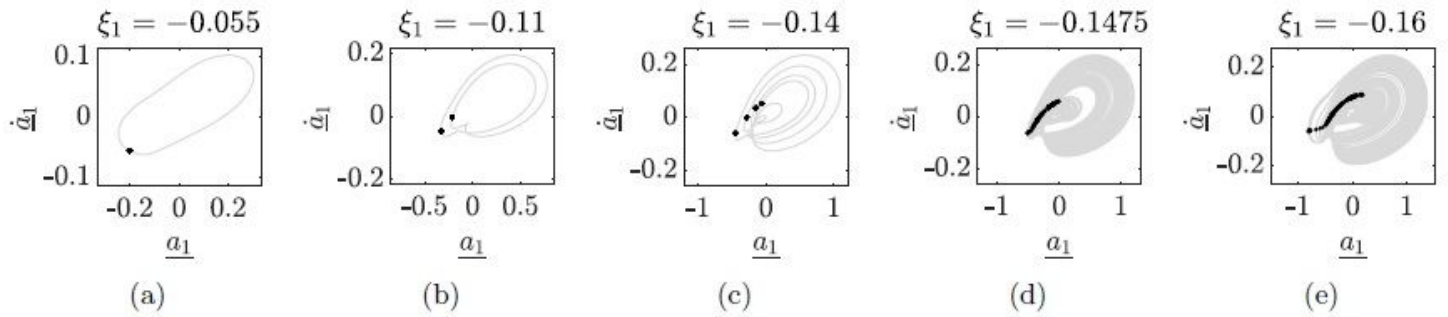


Figure 8

(see Manuscript file for figure legend)

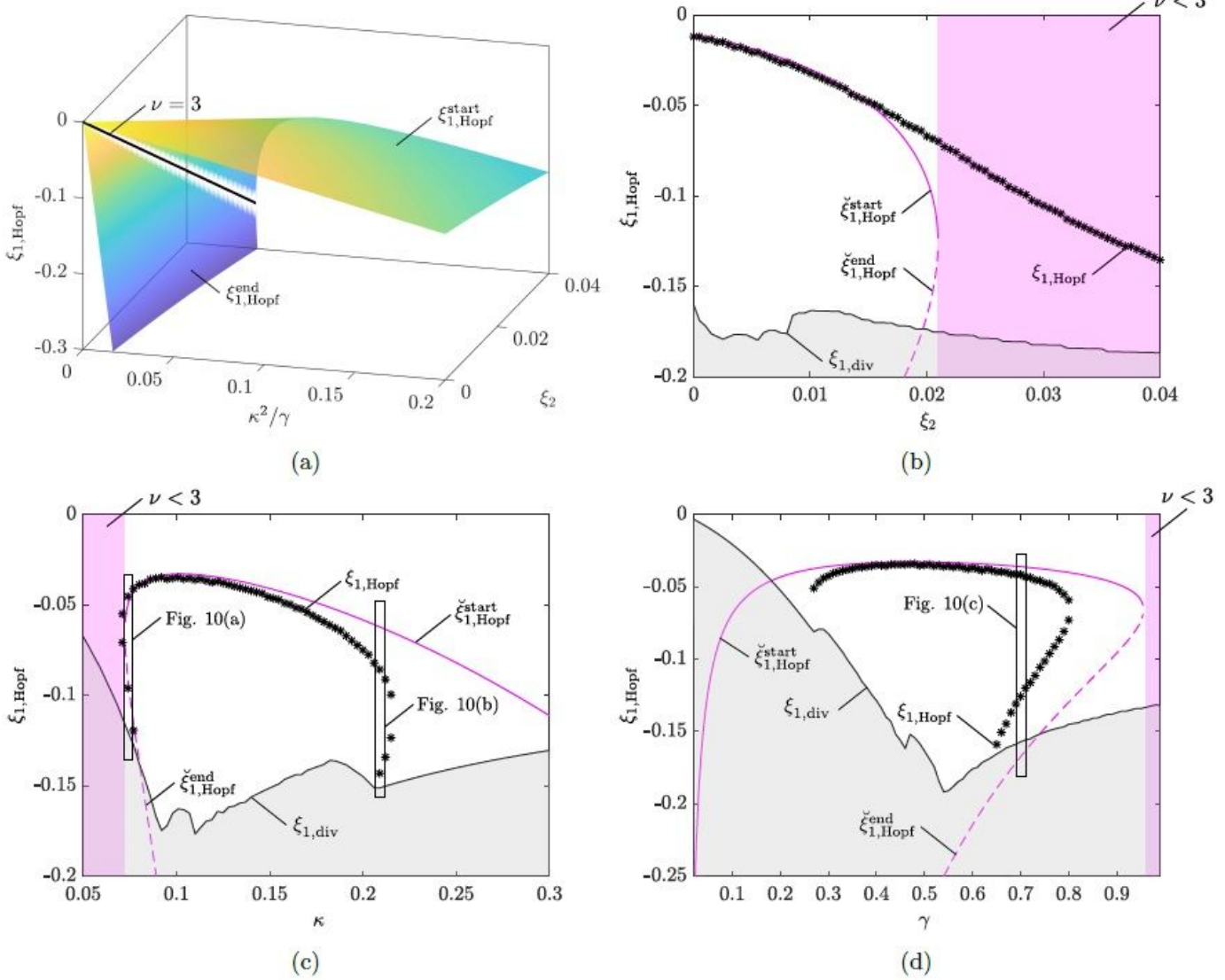


Figure 9

(see Manuscript file for figure legend)

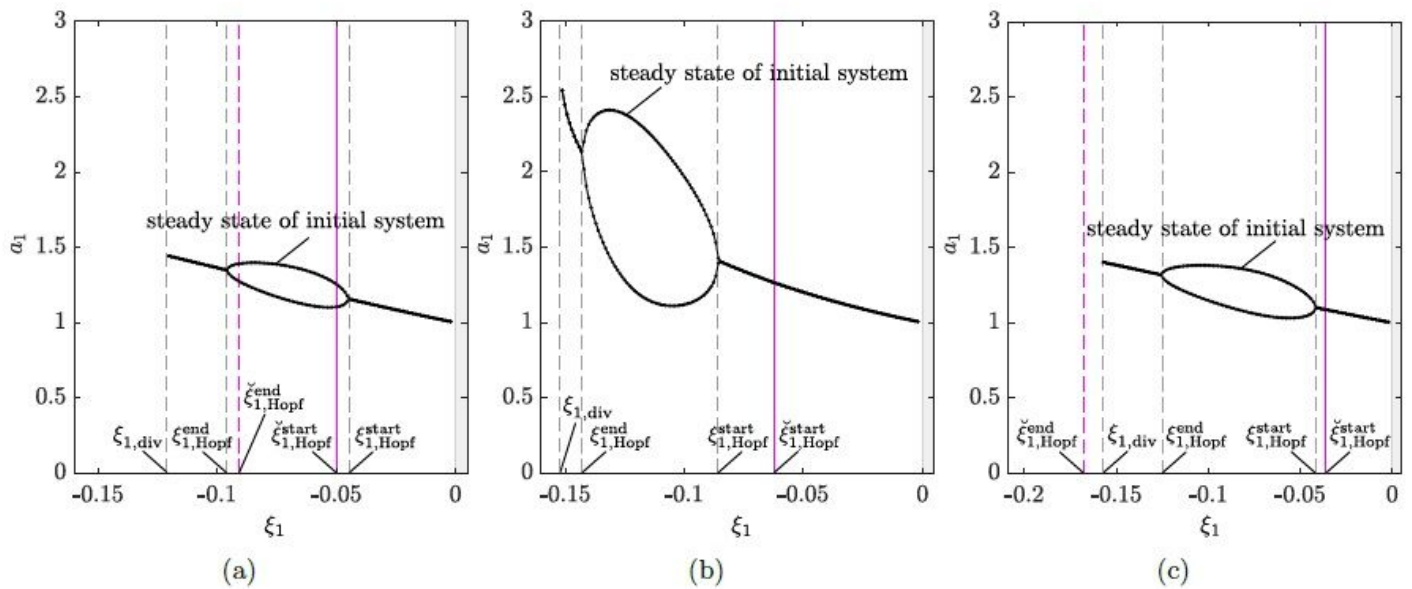


Figure 10

(see Manuscript file for figure legend)